Perpendicular magnetic anisotropy in Bi-substituted yttrium iron garnet films

Sreeveni Das,[1] Rhodri Mansell,[1, a)] Lukáš Flajšman,[1] Lide Yao,[1] and Sebastiaan van Dijken[1, b)]

NanoSpin, Department of Applied Physics, Aalto University School of Science, PO Box 15100, FI-00076 AALTO, Finland

Magnetic garnet thin films exhibiting perpendicular magnetic anisotropy (PMA) and ultra-low damping have recently been explored for applications in magnonics and spintronics. Here we present a systematic study of PMA and magnetic damping in bismuth-substitued yttrium iron garnet (Bi-YIG) films grown on sGGG (111) substrates by pulsed laser deposition (PLD). Films with thicknesses ranging from 5 nm to 160 nm are investigated. Structural characterization using X-ray diffraction and reciprocal space mapping demonstrates the pseudomorphic growth of the films. The films exhibit perpendicular magnetic anisotropy up to 160 nm thickness, with the zero-magnetic field state changing from fully saturated for low thicknesses to a dense magnetic stripe pattern for thicker films. The films show a ferromagnetic resonance (FMR) linewidth of 100 - 200 MHz with a Gilbert damping constant of the order of 4×10^{-3}. The broad FMR linewidth is caused by inhomogeneities of magnetic properties on micrometer length scales.

I. INTRODUCTION

Magnetic thin films with strong perpendicular magnetic anisotropy (PMA) are desirable for magnetic memory and logic devices. The recent development of perpendicularly magnetized spin-orbit torque based magnetic random access memory (SOT-MRAM)[1,2] is a prime example of the significance of PMA materials for spintronic applications. They offer low switching currents and fast switching responses due to strong PMA and high spin-orbit torque efficiency. Effective control of PMA is also attractive in racetrack memory designs and logic devices based on chiral spin textures[3–7]. However, the performance of these devices is often limited by slow magnetization dynamics and resistive losses. In this context, insulating magnetic garnets combining low Gilbert damping (α) and PMA have attracted interest as a replacement for ferromagnetic metals used in conventional spintronic devices. For example, PMA garnets can be integrated into domain wall racetracks where the domain wall motion is manipulated by magnon induced spin-transfer torque[8,9] or in spin-wave logic devices utilizing the isotropic excitation of magnetostatic forward volume mode (MSFVM) spin waves[10,11].

Yttrium ion garnet (YIG) is a versatile magnetic garnet with ultralow damping which has been widely studied due to its long spin wave propagation length[12,13]. YIG grown on lattice matched substrates exhibits an in-plane magnetic easy axis dominated by shape anisotropy. To achieve PMA, YIG films can be grown on garnet substrates with a larger lattice constant such as sGGG[14,15], YSGG[16], and GSGG[17]. A relatively large strain is required to achieve PMA in YIG films and the observation of PMA is limited to thicknesses below 50 nm[15]. One solution to this issue is doping YIG with strong spin-orbit coupling elements such as Bi[18–21], Mn[22], Ce[23,24] and Ga[25]. This results in tunable magnetic anisotropy and

in some cases, enhanced magneto-optical properties[24,26]. PMA is also reported in rare-earth iron garnet films including thulium iron garnet (TmIG), europium iron garnet (EuIG), and terbium iron garnet (TbIG)[27–30]. Such thin films can also possess the Dzyaloshinskii-Moriya interaction (DMI) which gives rise to chiral magnetic textures that are of significant current interest for device applications[31–33]. However, the damping of rare-earth iron garnets is relatively high, comparable to that of ferromagnetic metals.

In this work, we investigate PMA and magnetic damping in Bi-YIG films with different thicknesses on sGGG(111) substrates. Fully-strained pseudomorphic growth is demonstrated up to a thickness of 160 nm, resulting in fully out-of-plane magnetized films up to a thickness of ~ 140 nm with a Gilbert damping parameter of $\sim 4 \times 10^{-3}$. The films show broad FMR linewidth (100 - 200 MHz) due to local inhomogeneities of magnetic properties.

II. EXPERIMENTAL METHODS

Bi-YIG films were grown on (Mg,Zr)-substituted GGG(111) substrates by pulsed laser deposition (PLD) using a KrF laser ($\lambda = 248$ nm) from a stoichiometric target of composition $Bi_1Y_2Fe_5O_{12}$. Growth conditions were systematically optimized to ensure crystallinity of the films. Before deposition, the substrates were annealed at 700 °C in 10 mbar oxygen. The films were grown at 600 °C in 0.05 mbar oxygen. After deposition, the films were annealed at 700 °C in 100 mbar oxygen for 30 minutes to enhance their crystallinity and stoichiometry. *In-situ* reflection high energy electron diffraction (RHEED) was used to monitor the growth of the films. RHEED intensity oscillations were not observed during growth, however, a clear diffraction pattern was observed after post-deposition annealing. Bi-YIG films with thicknesses ranging from 5 nm to 160 nm were investigated.

The crystalline structure of the Bi-YIG films was characterized using high resolution X-ray diffraction (XRD) measurements and the strain distribution of the films was

———————————

a)Corresponding author: rhodri.mansell@aalto.fi

b)Corresponding author: sebastiaan.vandijken@aalto.fi

analyzed by X-ray reciprocal space mapping (RSM). Film thicknesses were determined by X-ray reflectivity (XRR) measurements. Atomic force microscopy (AFM) measurements were carried out to study the homogeneity and roughness of the films.

The static magnetic properties of the Bi-YIG films were characterized using magneto-optical Kerr effect (MOKE) microscopy, magnetic force microscopy (MFM), and vibrating sample magnetometry (VSM). The dynamic magnetic properties of the films were determined through ferromagnetic resonance (FMR) measurements using a broadband vector network analyzer (VNA) in a flip-chip geometry. Super-Nyquist sampling magneto-optical Kerr effect (SNS-MOKE) microscopy was used to study the spatial variation of the magnetization dynamics.

Additionally, elemental mappings of the films were performed by energy dispersive X-ray spectroscopy (EDX) in longitudinal and cross-sectional geometry. Microstructure and morphology of the Bi-YIG films were inspected by high resolution scanning transmission electron microscopy (STEM, JEOL 2200FS) with double Cs- correctors. For that, the cross-sectional lamellas were prepared by focused ion beam (FIB) cutting on a multibeam system (JEOL JIB 4700F).

III.   RESULTS AND DISCUSSION

A.   Structural characterization

XRD θ-2θ scans of Bi-YIG films on sGGG with thicknesses ranging from 5 nm to 160 nm are shown in Fig. 1. In each scan, the sGGG(444) substrate peak is seen around 50.5° with the Bi-YIG film peak showing up as a shoulder for thinner films and as a distinct peak
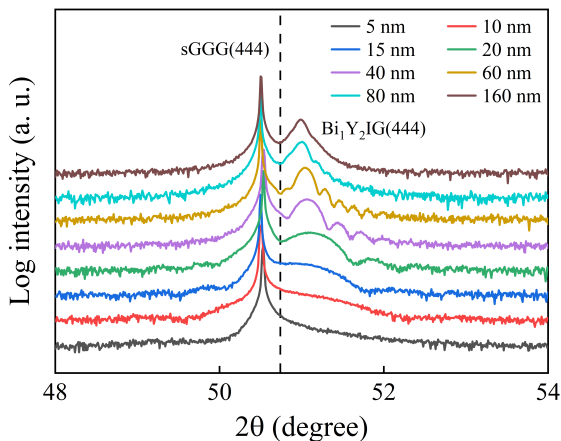
for thicker films. The vertical dashed line marks the expected position of the bulk $Bi_1Y_2IG(444)$ diffraction peak[18,34]. The diffraction peak of the Bi-YIG films is located at a higher angle than the expected bulk position, indicating that the films are grown under compressive out-of-plane strain (i.e., tensile in-plane strain). This is consistent with the lattice mismatch between Bi-YIG (12.45 Å)[18,34] and sGGG (12.49 Å) which is expected to induce tensile strain in the plane of the Bi-YIG films, as seen in previous investigations of the system[18–21]. The films are crystalline and their surface is reasonably smooth as demonstrated by clear Laue fringes in the XRD scans of films with thicknesses ranging from 20 nm to 80 nm.

Figures 2(a) and 2(b) show the reciprocal space maps along the (642) oblique plane for Bi-YIG films with a thickness of 20 nm and 160 nm, respectively. In these two cases, as for all the films, the film peak is vertically aligned with the substrate peak, confirming that the films are coherently grown onto the sGGG substrate. The position of the film peak at higher Q_z compared to the substrate peak in the RSMs shows the out-of-plane lattice compression consistent with the θ-2θ scans in Fig. 1.
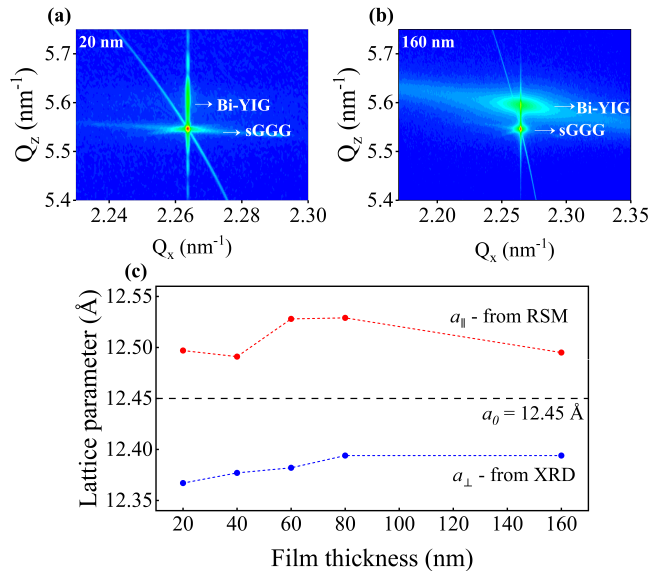

FIG. 2: Reciprocal space maps of films with a thickness of (a) 20 nm and (b) 160 nm. (c) In-plane ($a_\parallel$) and out-of-plane ($a_\perp$) lattice parameters of the Bi-YIG films as a function of thickness extracted from RSM and θ-2θ measurements, respectively. The lattice constant of bulk Bi_1Y_2IG ($a_0 = 12.45$ Å) is indicated by the horizontal dashed line.

The out-of-plane lattice parameter $a_\perp$ extracted from the θ-2θ scans and the in-plane lattice parameter $a_\parallel$ extracted from the RSMs are plotted as a function of film thickness in Fig. 2(c). $a_\parallel$ is greater than a_0 for all thicknesses, confirming the tensile in-plane strain. An increase

FIG. 1: XRD θ-2θ scans of Bi-YIG films on sGGG for film thicknesses ranging from 5 nm to 160 nm. The scans are vertically offset for clarity.

in $a_\perp$ is observed with film thickness, however, it does not approach the bulk lattice constant a_0 even for the thickest film. This demonstrates that even for thicknesses over 100 nm the film strain does not relax fully.

Since all the films show pseudomorphic growth characteristics, the lattice parameter of the relaxed structure (a_0) can be derived from $a_\parallel$ and $a_\perp$ of the strained films using the following formula[35],

$$a_0 = a_\parallel - \frac{\mu - 1}{1 + \mu}(a_\perp - a_\parallel), \quad (1)$$

where $\mu = 0.29$ is the Poisson coefficient of the material[36]. The lattice parameter of the relaxed structure (a_0) thus calculated for different film thicknesses varies from 12.42 Å to 12.44 Å. The calculated a_0 is smaller than the expected value of 12.45 Å. According to Vegard's law, this suggests around 20 % to 50 % lower Bi concentration in the films[37] than the nominal value. The relative abundance of Bi and Y in a 160 nm thick Bi-YIG film estimated by EDX also indicates a lower Bi to Y ratio in the films (See supplementary note 1).

The surface roughness of the films, measured by atomic force microscopy (AFM) and X-ray reflectivity (XRR) measurements, is low and only gradually increases with film thickness from 0.3 nm for the 5 nm thick film to 2.2 nm for the 160 nm thick film (See supplementary note 2). The low surface roughness is consistent with the observation of Laue oscillations in the XRD scans shown in Fig. 1.
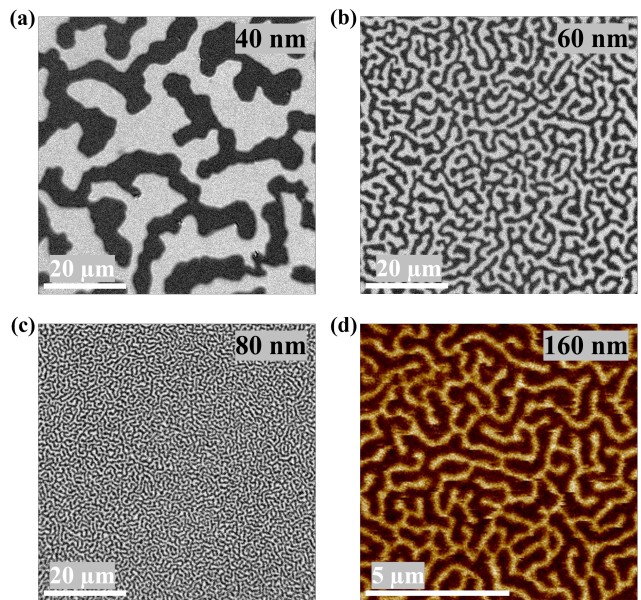
FIG. 4: Magnetic stripe domain pattern at zero magnetic field after demagnetization for Bi-YIG films with a thickness of (a) 40 nm, (b) 60 nm, and (c) 80 nm obtained by MOKE microscopy. (d) MFM image of the stripe domain pattern at zero magnetic field for a 160 nm thick film.

B. Magnetic characterization

Polar MOKE hysteresis loops shown in Fig. 3 confirm the PMA of the Bi-YIG films. The combination of in-plane tensile strain and the negative magnetostriction coefficient of Bi-YIG in the (111) direction promotes PMA in the films by inducing a magnetoelastic anisotropy. Preferential Bi occupation of Y sites may also lead to an additional growth-induced perpendicular anisotropy term[18,20]. Films with thicknesses up to 20 nm show square hysteresis loops, with the 5 nm film, shown in Fig. 3(a) having a coercivity of around 0.2 mT. The hysteresis of thicker films is more rounded because of the formation of magnetic stripe domains at low magnetic fields. The thicker films also show considerably increased out-of-plane saturation fields. The magnetic domain structure of Bi-YIG films with thicknesses 40 nm, 60 nm, 80 nm, and 160 nm imaged at zero applied magnetic field after demagnetization are shown in Fig. 4 (note the different scale bars). Figures 4(a)-(c) were recorded using MOKE microscopy and Fig. 4(d) was recorded using MFM. A decrease in the width of the stripe domains is observed with increasing film thickness.

The dynamic magnetic properties of the Bi-YIG films were studied with broadband FMR spectroscopy using a vector network analyzer (VNA). The samples are placed face-down onto a coplanar waveguide (CPW), and a static magnetic field is applied perpendicular to the film plane. The transmission coefficient (S_{21}) of the CPW/Bi-
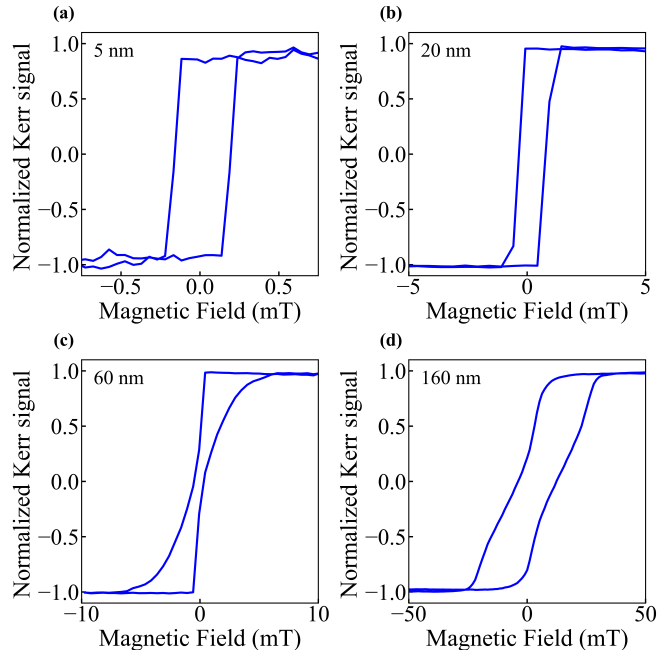

FIG. 3: Polar MOKE hysteresis loops under out-of-plane applied magnetic fields of Bi-YIG films with a thickness of (a) 5 nm, (b) 20 nm, (c) 60 nm, and (d) 160 nm. Note the different magnetic field scales in each plot.

Thickness (nm)	$\mu_0 M_{\text{eff}}$ (mT)	α ($\times 10^{-3}$)	Δf_0 (MHz)	$\mu_0 M_{\text{s}}$ (mT)	$\mu_0 H_{\text{Ku}}$ (mT)	K_{u} (kJ/m^3)	K_{eff} (kJ/m^3)
20	-91	5.4	110	75	166	5.0	2.7
40	-60	5.5	150	99	159	6.3	2.4
60	-52	3.9	120	78	130	4.0	1.6
80	-30	5.0	180	81	111	3.6	1.0
160	9	4.3	220	76	67	2.0	-0.3

TABLE I: $\mu_0 M_{\text{eff}}$, α and Δf_0 derived from FMR measurements, $\mu_0 M_{\text{s}}$ derived from VSM measurements, and the extracted values of $\mu_0 H_{\text{Ku}}$, K_{u} and K_{eff} for Bi-YIG films with different thicknesses.

YIG structure is measured as a function of frequency at a fixed external magnetic field. Fig. 5(a) shows representative FMR spectra at different magnetic fields for a Bi-YIG film with a thickness of 20 nm. The FMR frequency (f_{res}) and inhomogeneous linewidth (Δf) are determined by fitting the S_{21} data with a Lorentzian curve, where Δf refers to the full width at half maximum of the Lorentzian peak (See supplementary note 3). The effective magnetization, M_{eff}, is then extracted by numerically fitting the field dependence of f_{res} using the Kittel equation for a perpendicular measurement geometry:

$$f_{\text{res}} = \frac{\mu_0 \gamma}{2\pi}(H - M_{\text{eff}}), \qquad (2)$$

where μ_0 is the vacuum permeability and γ is the gyromagnetic ratio. The Gilbert damping parameter, α, is estimated by numerically fitting the frequency dependence of Δf using the equation,

$$\Delta f = 2\alpha f + \Delta f_0. \qquad (3)$$

Here, Δf_0 denotes the linewidth broadening due to the spatial inhomogeneity of the film. Figures 4(b) and 4(c) show representative fits to f_{res} vs H and Δf vs f data, respectively, for a Bi-YIG film with a thickness of 20 nm.

Table I summarizes M_{eff}, α, and Δf_0 extracted from FMR measurements for Bi-YIG films with thicknesses ranging from 20 nm to 160 nm. The Gilbert damping parameter α is similar for all the films at around 4×10^{-3}.

To quantify the anisotropy strength, we deduced the anisotropy field H_{Ku}, uniaxial anisotropy K_{u} and the effective anisotropy K_{eff} from the effective magnetization (M_{eff}) using the following formulas:

$$\begin{aligned} H_{\text{Ku}} &= M_{\text{s}} - M_{\text{eff}} \\ K_{\text{u}} &= \frac{\mu_0 H_{\text{Ku}} M_{\text{s}}}{2} \\ K_{\text{eff}} &= K_{\text{u}} - \frac{\mu_0 M_{\text{s}}^2}{2} \end{aligned} \qquad (4)$$

where the saturation magnetization M_{s} is estimated from vibrating sample magnetometry (VSM) measurements with out-of-plane magnetic field. By the definition of K_{eff} in equation (4), the sign of K_{eff} determines the spin orientation. When K_{eff} changes sign, a spin reorientation

between out-of-plane and in-plane magnetized states occurs. H_{Ku}, M_{s}, K_{u}, and K_{eff} extracted for different film thicknesses are summarized in Table I.

K_{u} is positive for all the films confirming strong PMA up to 160 nm thickness. This is consistent with the XRD and RSM results and demonstrates the robustness of the growth-induced strain and strain-induced PMA in our Bi-YIG films. Because of a gradual relaxation of strain with film thickness (Fig. 2(c)), K_{u} decreases in the thicker films. M_{s} of the Bi-YIG films is notably smaller than that of YIG ($\mu_0 M_{\text{s}} = 180$ mT)[38] and previous measurements of Bi-YIG[18]. The relatively low M_{s} likely explains why the easy axis of magnetization is oriented out-of-plane up to large film thicknesses since the demagnetization energy favoring in-plane magnetization is relatively small. For the 160 nm thick film, M_{eff} is positive and K_{eff} is negative, implying that the preferred orientation of magnetization is in-plane. However, be-
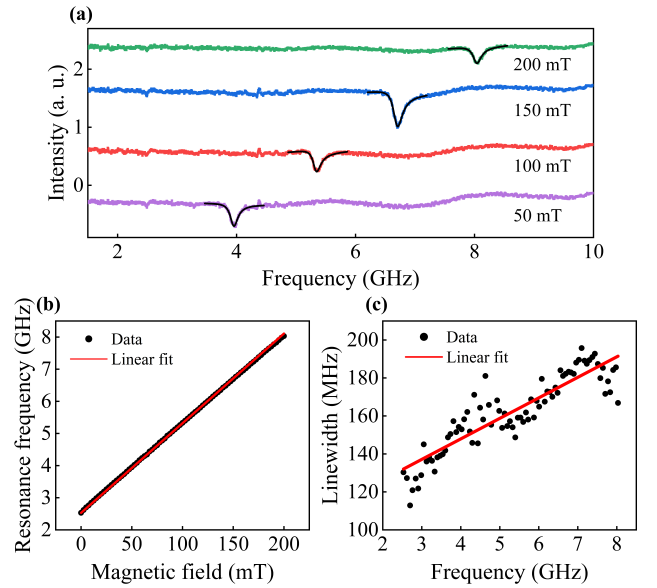

FIG. 5: (a) FMR spectra recorded with different external magnetic fields on a 20 nm thick Bi-YIG film. The black curves are Lorentz fits to the FMR resonance. For clarity, a vertical offset is applied to the spectra. (b) Fit of $f_{\text{res}}(H)$ and (c) fit of $\Delta f(f)$ of the same film.
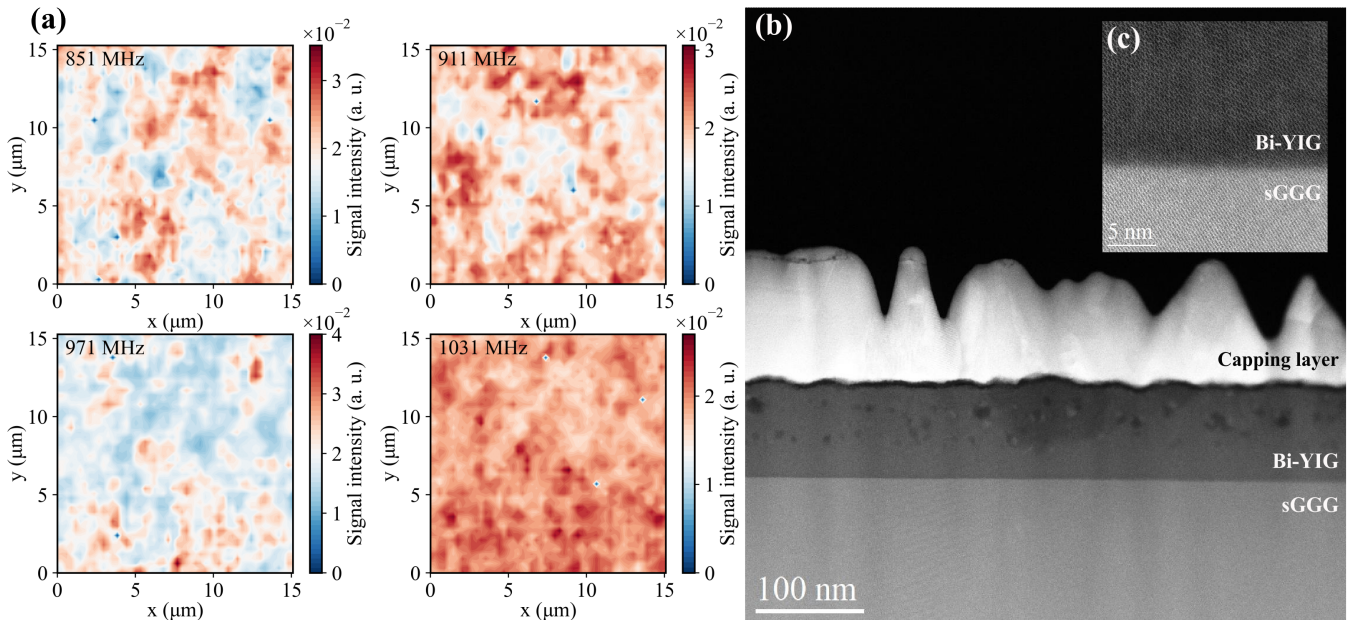
FIG. 6: (a) Spatial mapping of the dynamic magnetic response for a Bi-YIG film with a thickness of 80 nm at different RF frequencies recorded using SNS-MOKE microscopy. The intensity is proportional to the local maximum deviation of the out-of-plane component of the magnetization. (b), (c) Cross-sectional HAADF-STEM images for the same film.

cause the effective anisotropy is small, a perpendicular magnetic stripe domain still forms when the film is demagnetized by a perpendicular magnetic field (Fig. 4(d)). The decrease in stripe domain width at zero magnetic field (Fig. 4) for thicker films, is also consistent with a reducing effective magnetic anisotropy. The sign change of K_{eff} with increasing film thickness suggests that the spin reorientation transition occurs at around 140 nm in our Bi-YIG films.

The excitation and detection of MSFVM spin waves in low-damping Bi-YIG films with large PMA is desirable for potential device applications. However, despite having low magnetic damping, spin wave propagation is not observed in our Bi-YIG films (See supplementary note 4 for experimental details), which is likely due to the relatively high inhomogeneous linewidth broadening of the films. The Gilbert damping parameter α estimated from the frequency dependence of the FMR linewidth does not solely affect the propagation of spin waves. To investigate this further, we used a home-built SNS-MOKE[39] microscope to probe the spatial variation of the FMR for a film with a thickness of 80 nm. In the measurements, an external magnetic field of 50 mT is applied parallel to the film plane, and the magnetization dynamics is excited by a spatially homogeneous RF field generated by an omega antenna placed above the film. For different excitation frequencies, the film was scanned over an area of 15×15 μm^2 in steps of 0.3 μm and the magnitude of the average dynamic magnetization was recorded. Figure 6(a)

shows spatial maps of the dynamic magnetic response of the film at different RF frequencies. The intensity variation across different regions in Fig. 6(a) is due to local changes in the FMR frequency, suggesting inhomogeneities of the magnetic properties. The FMR frequency is sensitive to local changes in both the saturation magnetization and the uniaxial anisotropy which can lead to particularly large inhomogeneous broadening in perpendicularly magnetized films. Here, local shifts in the spin wave dispersion caused by magnetic inhomogeneities are large enough to prevent spin wave propagation even with relatively low magnetic damping.

We performed cross-sectional high-angle annular dark field (HAADF) STEM imaging to examine the origin of the magnetic inhomogeneities. Figures 6(b) and 6(c) show HAADF-STEM images from a film with a thickness of 80 nm. The interface between sGGG and Bi-YIG, shown in Fig. 6(c), is sharp and nearly perfect, indicating that interfacial defects and dislocations are absent. However, in Fig. 6(b), a variation in dark-field imaging contrast is observed in some parts of the film away from the substrate interface. The areas with dark contrast exhibit a different composition. The changes in the distribution of oxygen (O) and iron (Fe) within the regions with dark contrast, as revealed by STEM-EDX analysis, align with this observation (See supplementary note 3). The observed compositional changes do not lead to visible changes in the lattice as verified by the high-resolution HAADF-STEM imaging (See supplementary

note 4). Film areas that are iron deficient are likely responsible for the low saturation magnetization found in these films. While the scale of the STEM images is too small to study property changes on the scales relevant to the inhomogeneities seen in Fig. 6(a), the structural imperfections on sub-micrometer length scales do likely contribute to the inhomogeneous magnetic properties that result in broad FMR linewidths.

IV. CONCLUSION

In this study, structural and magnetic characterization of PLD-grown Bi-YIG films on sGGG was carried out for film thicknesses ranging from 5 nm to 160 nm. All the Bi-YIG films are strained coherently by the sGGG substrate and exhibit strong PMA. Polar MOKE measurements indicate full remanence for small film thickness and dense stripe domains with perpendicular magnetization for the thicker films. The PMA gradually decreases with film thickness, leading to a spin reorientation transition around 140 nm. The magnetic damping parameter for films with perpendicular magnetization is around 4×10^{-3} irrespective of film thickness. Finally, the absence of spin wave propagation despite low damping is attributed to the spatial inhomogeneities of the magnetic properties leading to variations in the dispersion of spin waves.

SUPPLEMENTARY MATERIAL

The supplementary material contains further details of sample characterization by EDX, AFM and STEM, as well as discussion of the FMR fitting and spin wave propagation experiments.

ACKNOWLEDGMENTS

DATA AVAILABILITY

The data that support the findings of this study are available from the corresponding author upon reasonable request.

[1] B. Dieny and M. Chshiev, "Perpendicular magnetic anisotropy at transition metal/oxide interfaces and applications," Reviews of Modern Physics **89**, 025008 (2017).

[2] M. Cubukcu, O. Boulle, N. Mikuszeit, C. Hamelin, T. Brächer, N. Lamard, M. C. Cyrille, L. Buda-Prejbeanu, K. Garello, I. M. Miron, O. Klein, G. de Loubens, V. V. Naletov, J. Langer, B. Ocker, P. Gambardella, and G. Gaudin, "Ultra-fast perpendicular spin–orbit torque MRAM," IEEE Transactions on Magnetics **54**, 1–4 (2018).

[3] Y. Zhang, W. Zhao, J. O. Klein, C. Chappert, and D. Ravelosona, "Peristaltic perpendicular-magnetic-anisotropy racetrack memory based on chiral domain wall motions," Journal of Physics D: Applied Physics **48**, 105001 (2015).

[4] R. Tomasello, E. Martinez, R. Zivieri, L. Torres, M. Carpentieri, and G. Finocchio, "A strategy for the design of skyrmion racetrack memories," Scientific Reports **4** (2014).

[5] W. Kang, Y. Huang, C. Zheng, W. Lv, N. Lei, Y. Zhang, X. Zhang, Y. Zhou, and W. Zhao, "Voltage controlled magnetic skyrmion motion for racetrack memory," Scientific Reports **6** (2016).

[6] X. Zhang, M. Ezawa, and Y. Zhou, "Magnetic skyrmion logic gates: conversion, duplication and merging of skyrmions," Scientific Reports **5** (2015).

[7] S. H. C. Baek, K. W. Park, D. S. Kil, Y. Jang, J. Park, K. J. Lee, and B. G. Park, "Complementary logic operation based on electric-field controlled spin–orbit torques," Nature Electronics **1**, 398–403 (2018).

[8] J. Han, P. Zhang, J. T. Hou, S. A. Siddiqui, and L. Liu, "Mutual control of coherent spin waves and magnetic domain walls in a magnonic device," Science **366**, 1121–1125 (2019).

[9] Y. Fan, M. J. Gross, T. Fakhrul, J. Finley, J. T. Hou, S. Ngo, L. Liu, and C. A. Ross, "Coherent magnon-induced domain-wall motion in a magnetic insulator channel," Nature Nanotechnology (2023).

[10] S. Klingler, P. Pirro, T. Brächer, B. Leven, B. Hillebrands, and A. V. Chumak, "Spin-wave logic devices based on isotropic forward volume magnetostatic waves," Applied Physics Letters **106** (2015).

[11] O. Zografos, S. Dutta, M. Manfrini, A. Vaysset, B. Sorée, A. Naeemi, P. Raghavan, R. Lauwereins, and I. P. Radu, "Non-volatile spin wave majority gate at the nanoscale," AIP Advances **7** (2017).

[12] C. Liu, J. Chen, T. Liu, F. Heimbach, H. Yu, Y. Xiao, J. Hu, M. Liu, H. Chang, T. Stueckler, S. Tu, Y. Zhang, Y. Zhang, P. Gao, Z. Liao, D. Yu, K. Xia, N. Lei, W. Zhao, and M. Wu, "Long-distance propagation of short-wavelength spin waves," Nature Communications **9** (2018).

[13] A. A. Serga, A. V. Chumak, and B. Hillebrands, "YIG magnonics," Journal of Physics D: Applied Physics **43**, 264002 (2010).

[14] J. Fu, M. Hua, X. Wen, M. Xue, S. Ding, M. Wang, P. Yu, S. Liu, J. Han, C. Wang, H. Du, Y. Yang, and J. Yang, "Epitaxial growth of $Y_3Fe_5O_{12}$ thin films with perpendicular magnetic anisotropy," Applied Physics Letters **110**, 202403 (2017).

[15] S. Chen, Y. Xie, Y. Yang, D. Gao, D. Liu, L. Qin, W. Yan, B. Tan, Q. Chen, T. Gong, E. Li, L. Bi, T. Liu, and L. Deng, "The 50 nm-thick yttrium iron garnet films with perpendicular magnetic anisotropy," Chinese Physics B **31**, 048503 (2022).

[16] G. Li, H. Bai, J. Su, Z. Z. Zhu, Y. Zhang, and J. W. Cai, "Tunable perpendicular magnetic anisotropy in epitaxial $Y_3Fe_5O_{12}$ films," APL Materials **7**, 041104 (2019).

[17] J. Ding, C. Liu, Y. Zhang, U. Erugu, Z. Quan, R. Yu, E. McCollum, S. Mo, S. Yang, H. Ding, X. Xu, J. Tang, X. Yang, and M. Wu, "Nanometer-thick yttrium iron garnet films with perpendicular anisotropy and low damping," Physical Review Applied **14**, 014017 (2020).

[18] L. Soumah, N. Beaulieu, L. Qassym, C. Carrétéro, E. Jacquet, R. Lebourgeois, J. B. Youssef, P. Bortolotti, V. Cros, and A. Anane, "Ultra-low damping insulating magnetic thin films get perpendicular," Nature Communications **9**, 3355 (2018).

[19] X. Liu, Q. Yang, D. Zhang, Y. Wu, and H. Zhang, "Magnetic properties of bismuth substituted yttrium iron garnet film with perpendicular magnetic anisotropy," AIP Advances **9**, 115001 (2019).

[20] Y. Lin, L. Jin, H. Zhang, Z. Zhong, Q. Yang, Y. Rao, and M. Li, "Bi-YIG ferrimagnetic insulator nanometer films with large perpendicular magnetic anisotropy and narrow ferromagnetic resonance linewidth," Journal of Magnetism and Magnetic Materials **496**, 165886 (2020).

[21] Y. Jia, Z. Liang, H. Pan, Q. Wang, Q. Lv, Y. Yan, F. Jin, D. Hou, L. Wang, and W. Wu, "Bismuth doping enhanced tunability of strain-controlled magnetic anisotropy in epitaxial $Y_3Fe_5O_{12}$(111) films," Chinese Physics B **32**, 027501 (2023).

[22] C. T. Wang, X. F. Liang, Y. Zhang, X. Liang, Y. P. Zhu, J. Qin, Y. Gao, B. Peng, N. X. Sun, and L. Bi, "Controlling the magnetic anisotropy in epitaxial $Y_3Fe_5O_{12}$ films by manganese doping," Phys. Rev. B **96**, 224403 (2017).

[23] E. Lage, L. Beran, A. U. Quindeau, L. Ohnoutek, M. Kucera, R. Antos, S. R. Sani, G. F. Dionne, M. Veis, and C. A. Ross, "Temperature-dependent Faraday rotation and magnetization reorientation in cerium-substituted yttrium iron garnet thin films," APL Materials **5**, 036104 (2017).

[24] M. Kuila, A. Sagdeo, L. A. Longchar, R. J. Choudhary, S. Srinath, and V. R. Reddy, "Robust perpendicular magnetic anisotropy in Ce substituted yttrium iron garnet epitaxial thin films," Journal of Applied Physics **131**, 203901 (2022).

[25] T. Böttcher, M. Ruhwedel, K. O. Levchenko, Q. Wang, H. L. Chumak, M. A. Popov, I. V. Zavislyak, C. Dubs, O. Surzhenko, B. Hillebrands, A. V. Chumak, and P. Pirro, "Fast long-wavelength exchange spin waves in partially compensated Ga:YIG," Applied Physics Letters **120**, 102401 (2022).

[26] D. Lacklison, G. Scott, H. Ralph, and J. Page, "Garnets with high magnetooptic figures of merit in the visible region," IEEE Transactions on Magnetics **9**, 457–460 (1973).

[27] C. N. Wu, C. C. Tseng, Y. T. Fanchiang, C. K. Cheng, K. Y. Lin, S. L. Yeh, S. R. Yang, C. T. Wu, T. Liu, M. Wu, M. Hong, and J. Kwo, "High-quality thulium iron garnet films with tunable perpendicular magnetic anisotropy by off-axis sputtering – correlation between magnetic properties and film strain," Scientific Reports **8** (2018).

[28] E. R. Rosenberg, L. Beran, C. O. Avci, C. Zeledon, B. Song, C. Gonzalez-Fuentes, J. Mendil, P. Gambardella, M. Veis, C. Garcia, G. S. D. Beach, and C. A. Ross, "Magnetism and spin transport in rare-earth-rich epitaxial terbium and europium iron garnet films," Physical Review Materials **2**, 094405 (2018).

[29] V. H. Ortiz, M. Aldosary, J. Li, Y. Xu, M. I. Lohmann, P. Sellappan, Y. Kodera, J. E. Garay, and J. Shi, "Systematic control of strain-induced perpendicular magnetic anisotropy in epitaxial europium and terbium iron garnet thin films," APL Materials **6**, 121113 (2018).

[30] J. J. Bauer, E. R. Rosenberg, and C. A. Ross, "Perpendicular magnetic anisotropy and spin mixing conductance in polycrystalline europium iron garnet thin films," Applied Physics Letters **114** (2019).

[31] L. Caretta, E. Rosenberg, F. Büttner, T. Fakhrul, P. Gargiani, M. Valvidares, Z. Chen, P. Reddy, D. A. Muller, C. A. Ross, and G. S. D. Beach, "Interfacial Dzyaloshinskii-Moriya interaction arising from rare-earth orbital magnetism in insulating magnetic oxides," Nature Communications **11**, 1090 (2020).

[32] H. Wang, J. Chen, T. Liu, J. Zhang, K. Baumgaertl, C. Guo, Y. Li, C. Liu, P. Che, S. Tu, S. Liu, P. Gao, X. Han, D. Yu, M. Wu, D. Grundler, and H. Yu, "Chiral spin-wave velocities induced by all-garnet interfacial Dzyaloshinskii-Moriya interaction in ultrathin yttrium iron garnet films," Physical Review Letters **124**, 027203 (2020).

[33] S. Vélez, S. Ruiz-Gómez, J. Schaab, E. Gradauskaite, M. S. Wörnle, P. Welter, B. J. Jacot, C. L. Degen, M. Trassin, M. Fiebig, and P. Gambardella, "Current-driven dynamics and ratchet effect of skyrmion bubbles in a ferrimagnetic insulator," Nature Nanotechnology **17**, 834–841 (2022).

[34] M. Niyaifar, Ramani, M. C. Radhakrishna, A. Hassnpour, M. Mozaffari, and J. Amighian, "The correlation of lattice constant with superexchange interaction in Bi-YIG fabricated by mechanochemical processing," in *ICAME 2007* (Springer Berlin Heidelberg, 2008) pp. 575–580.

[35] L. Soumah, *Pulsed Laser Deposition of Substituted thin Garnet Films for Magnonic Applications*, Ph.D. thesis, Université Paris-Saclay (2019).

[36] H. M. Chou and E. D. Case, "Characterization of some mechanical properties of polycrystalline yttrium iron garnet (YIG) by non-destructive methods," Journal of Materials Science Letters **7**, 1217–1220 (1988).

[37] I. Nadinov, O. Kovalenko, J. L. Rehspringer, M. Vomir, and L. Mager, "Limits of the magneto-optical properties of Bi:YIG films prepared on silica by metal organic decomposition," Ceramics International **45**, 21409–21412 (2019).

[38] A. Krysztofik, N. Kuznetsov, H. Qin, L. Flajšman, E. Coy, and S. van Dijken, "Tuning of magnetic damping in $Y_3Fe_5O_{12}$/metal bilayers for spin-wave conduit termination," Materials **15**, 2814 (2022).

[39] H. Qin, R. B. Holländer, L. Flajšman, F. Hermann, R. Dreyer, G. Woltersdorf, and S. van Dijken, "Nanoscale magnonic Fabry-Pérot resonator for low-loss spin-wave manipulation," Nature Communications **12** (2021).